Article

Not peer-reviewed version

Photodegradation of Pyridine in a Fluidized Bed Photocatalytic Reactor Using Pt-ZnO Supported on Al_2O_3 as a Catalyst

Ruby Gines , Carlos Montalvo * , Guadalupe Luna , Daniel Montalvo , Rosa M. Cerón , Julia G. Cerón ,
Sinuhe Ginés , Aracely García , Claudia A. Aguilar *

Posted Date: 23 June 2025

doi: 10.20944/preprints202506.1830.v1

Keywords: Photodegradation; nanoparticles; photoreactor; photocatalysis; ZnO; pyridine

Article

Photodegradation of Pyridine in a Fluidized Bed Photocatalytic Reactor Using Pt-ZnO Supported on Al_2O_3 as a Catalyst

Ruby Gines [1], Carlos Montalvo [2,*], Guadalupe Luna [3], Daniel Montalvo [4], Rosa M. Ceron [2], Julia G. Ceron [2], Sinuhe Ginés [3] and Aracely García [5] and Claudia Aguilar [2]

[1] Facultad de Ciencias Químicas, Universidad Veracruzana, Oriente 6 No.1009, Col. Rafael Alvarado, C.P. 94340 Orizaba, Ver., México
[2] Faculty of Chemistry, Autonomous University of Carmen, Ciudad del Carmen, Campeche, C. P. 24180, México
[3] División de Estudios de Posgrado e Investigación, Instituto Tecnológico de Orizaba, Av. Oriente 9 No. 852, Col. Emiliano Zapata, C.P. 94320, Orizaba, Ver., México
[4] Academia de Ingeniería Bioquímica, Instituto Tecnológico Superior de Acayucan, Costera del Golfo Km 216.4, Acayucan, Ver., C.P. 96100, México
[5] Department of Chemistry, Division of Natural and Exact Sciences, University of Guanajuato. Noria Alta s/n, Col. Noria Alta C.P. 36050, Guanajuato, Gto., México
* Correspondence: c_montalvo10@hotmail.com; (Tel.:938 139 4386, C.M.R)

Abstract

The degradation of pyridine, considered one of the most polluting heterocycles used in industries, was performed. A fluidized bed photocatalytic reactor (FBR) with the catalyst Pt-ZnO/Al_2O_3 synthesized by precipitation and wet impregnation was used for its removal. FTIR, XRD, and SEM characterization were performed on the catalyst. The analyses confirmed the hexagonal structure of ZnO (average crystal size: 53.18 nm), the successful incorporation of Pt (increase to 57.21 nm), and a nano-rods morphology in Pt-ZnO favoring the photocatalytic activity. The kinetics followed the pseudo-first-order model ($R^2 > 0.95$), obtaining a value of $k_1 = 1.943 \times 10^{-3}$ min^{-1} (reaction constant) y $k_2 = 1.527 \times 10^{-3}$ L/mg (absorption constant), reaching pyridine removal of 57.7% at conditions (pH 4, 160 ppm pyridine, 100 g catalyst), validating the efficiency of the RFL to improve mass transfer and catalytic exposure. With the results obtained, it was demonstrated that the Pt-ZnO/Al_2O_3 catalyst possesses high stability and potential for the treatment of industrial wastewater contaminated with N-heterocycles.

Keywords: photodegradation; nanoparticles; photoreactor; photocatalysis; ZnO; pyridine

1. Introduction

Every year, millions of cubic meters of wastewater from municipal, industrial, and agricultural discharges are discharged into waterways, which are inadequately or not treated. Water pollution has a severe impact on ecosystems and human health, so new alternatives are needed to reduce or eliminate substances that harm the environment and, consequently, the human species. One of the most recalcitrant pollutants that industries use is N-heterocycles, generating a latent threat to our environment [1,2].

N-heterocycles are a category of highly harmful toxic compounds that are introduced into the natural environment through wastewater [3–5]. Pyridine (C_5H_5N) is a nitrogen-containing N-heterocycle compound present in wastewater from industries [3,6,7] found in coal tar, mineral oil, and plant alkaloids [8]. It is a colorless liquid that boils at 115.2°C and freezes at 41.6 °C. Its density, 0.9819 g / cm^3, is close to that of water [9,10].

Pyridine has an unpleasant pungent odor, is volatile, toxic, and flammable, and is classified as a priority pollutant according to the United States Environmental Protection Agency (EPA) [11] that can trigger mutagenic agents, carcinogens, and teratogenic effects on the human body [3,4,12,13]. Liquid pyridine evaporates in the air and mixes easily with water. If pyridine is released, it may take days, months, or several years to degrade into other compounds (Agency for Toxic Substances and Disease Registry ATSDR), causing irreversible damage to human health and environmental quality [13]. Unfortunately, pyridine is a compound challenging to replace as it is indispensable in various industrial processes, as it serves as a raw material in the production of pesticides, herbicides, dyes, explosives, and pharmaceuticals and is used as a chemical solvent in the paint and rubber industries [3,8,14].

Therefore, its degradation represents a challenge for treatment processes [8,15] because physical or chemical methods are costly, and biological treatments are often inefficient [15,16].

Advanced oxidation processes (AOPs) are an alternative for removing recalcitrant organic compounds [17–19]. One of the advanced oxidation processes is heterogeneous photocatalysis, which is one of the most efficient methods for degrading organic compounds [20] using semiconductor materials with high catalytic activity aided by an ultraviolet radiation source [19,21–23].

In the interfacial region between the excited solid and the solution, the reactions of destruction or removal of contaminants occur without the catalyst undergoing chemical changes. Excitation of the semiconductor can be by direct excitation of the semiconductor so that it absorbs the photons used in the process or by initial excitation of molecules adsorbed on the surface of the catalyst, which in turn are capable of injecting charges (electrons) into the semiconductor [22,24]. Three fundamental components are needed for a heterogeneous photocatalytic reaction to occur: A photon source (with appropriate wavelength), a catalytic surface (usually a semiconductor material), and an electron acceptor, which in many cases is oxygen from the air. The various parameters or operating conditions that influence the rate and yield of photocatalytic degradation reactions include temperature, catalyst mass, solution pH, light intensity, and oxidizing agent concentration [25,26].

A Fluidized Bed reactor (FBR) consists of circulating a fluid through a static bed of solid particles with a surface velocity sufficient to suspend the particles and make them behave as if they were fluid [25,26].

Fluidized Bed Reactors are effective wastewater treatment technologies because they are excellent contacting devices and have the potential to improve efficiency, enhance effectiveness, and improve energy efficiency if designed and used appropriately [27]. Although applying the Fluidized Bed Reactor in advanced oxidation processes is relatively new, the FBR has proven to be a practical reactor in advanced oxidation process applications. Some of the excellent characteristics of the reactor include low operating cost, high resistance to system disturbances, high mass transfer rates, and uniform mixing [25,27].

Zinc oxide (ZnO) is a new type of semiconductor material that has attracted considerable attention in the field of materials science due to its low cost and excellent properties catalytic, photochemical, and thermal stability properties [28]. Recent research has focused on evaluating changes in the properties of catalysts by modifying their structure with metallic and non-metallic materials to enhance their photocatalytic potential and sensitivity to visible and ultraviolet light [12,29,30], thereby improving their photocatalytic ability. Most studies have focused on the doping of silver and gold on ZnO, but few use ZnO nanoparticles doped with platinum nanoparticles [29,31,32].

Platinum group metals (PGMs), including rhodium (Rh), ruthenium (Ru), platinum (Pt), and palladium (Pd), are essential catalysts in automotive catalytic converters and advanced applications such as heterogeneous catalysis and fuel cells [33]. These materials have unique physicochemical properties, where the catalytic cycle optimizes the efficiency through the interaction between metallic Pt nanoparticles and highly dispersed Pt oxidic centers. In PGM catalysts, Rh acts primarily as a reductant, Pd as an oxidant, and Pt as a bifunctional catalyst [34].

The morphology of Pt nanoparticles directly influences their catalytic activity. Crystalline facets exposed on the surface of the nanocrystals, depending on their orientation and structure, enhance reactivity. Pt nanoparticles with octahedral, cubic, or spherical shapes, dispersed on inert supports, demonstrate variable catalytic performance due to their morphology and surface area [34].

MGPs are crucial in modern catalysis, with platinum standing out for its multifunctional catalytic properties. The key to their effectiveness lies in the molecular structure and morphology of their nanoparticles, factors that determine their performance in various technological applications [34].

The catalyst developed contains an active phase, ZnO-Pt, and supports a characteristic spherical alumina (Al_2O_3) shape. This support has been the subject of research and development for many years. Alumina exhibits a cubic crystal structure with a molecular weight of 103.235 g/mol and a molar volume of 25.575 cc/mol. The compound is composed of 96% SiO_2, with the remainder comprising other elements such as Fe, B_2O_3, Al_2O_3, and Na_2O or K_2O [35].

Al_2O_3 is the most used support for industrial hydrogenation catalysts due to its large specific surface area, concentrated pore distribution, and affordable price [36].

Different coordination states of aluminum have been observed to affect the electronic and geometric configuration of supported active components. However, there are few studies on this topic to date. Consequently, it remains unclear how different aluminum coordination affects surface acidity [35–37].

Therefore, in this research, the synthesis of a zinc oxide (ZnO) catalyst doped with Platinum (Pt) nanoparticles and supported on alumina (Al_2O_3) was carried out to utilize it as a material capable of degrading pyridine and thus minimizing the environmental impact it causes.

2. Results and Discussion

2.1. Photocatalyst Characterization

Figure 1 shows the superposition of the spectrum of zinc oxide (ZnO), zinc oxide doped with platinum nanoparticles (Pt-ZnO), and zinc oxide doped with platinum nanoparticles supported on alumina (Pt-ZnO/Al_2O_3). In the spectra, a broad and intense band can be observed from 3500 cm^{-1} to 3000 $cm^{-1,}$ characteristic of the water present in the sample and associated with O-H tensile and H-O-H bending motion, respectively [38,39]. At around 1400 $cm^{-1,}$ a band attributed to the tetrahedral molecule ammonium (NH_4) can be observed, thus inferring that the sample contains ammonium salts generated as a product during the synthesis.

In the platinum-doped and alumina-supported spectra, prominent bands can be observed at 1200- 1000 $cm^{-1,}$ which correspond to Pt-ZnO bonds [40]. The approximate bands at 604 cm^{-1} indicate the stretching of the Zn-O bond. The peak corresponding to 874 cm^{-1} is due to the formation of a tetrahedral coordination of Zn. The spectrum of the catalyst supported on alumina (Al_2O_3) presents Al-O bonds of $Al_2O_{3,}$ which are observed in the prominent peaks found between 554 cm^{-1} and 456 cm^{-1} [12,41]. The presence of characteristic Zn-O bands confirms the ZnO structure in all samples; however, changes in the ZnO bands are observed upon incorporation of Pt, which may indicate a modification in the crystal lattice due to the addition of the metal.

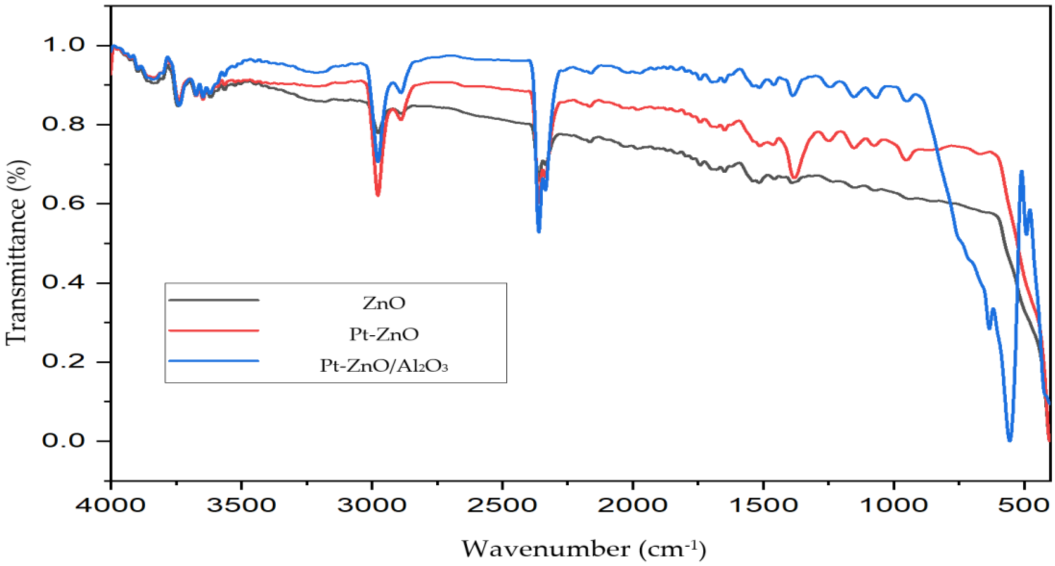

Figure 1. FTIR of the synthesis of ZnO, Pt-ZnO, and Pt-ZnO/Al_2O_3.

Figure 2 shows the results obtained from X-ray diffraction analysis of ZnO and Pt-ZnO nanoparticles. The highest peaks are found at 31.75° (1 0 0), 34.41° (0 0 2), 36. 23° (1 0 1), 47.51° (0 1 2), 56.57° (1 1 0), 62.81° (0 1 3), 66.35° (2 0 0), 67.91°(1 1 2), 69.05° (2 0 1), 72.55° (0 0 4), 76. 91° (2 0 2) crystal faceted planes of hexagonal ZnO wurtzite, according to the Crystallography Open Database (COD), demonstrating the formation of a hexagonal crystal structure. The value of the maximum peaks agrees with the COD-2300450 standard. The average crystallite size obtained was 53.17822 nm. The crystallite size depends on several factors, including intensity, peak broadening, sharpness, dislocation density, and deformation. The peaks are thin and well-defined, indicating high crystallinity of ZnO. There are no signs of amorphism or poorly crystallized phases.

Dislocation density is due to irregularities or cracks in the crystal structure. Increasing dislocation density increases deformation, which in turn decreases crystallite size. The results confirm that size is directly related to deformation and dislocation density. Peak displacement or peak broadening depends on the deformation present in the materials [42–44]. The result infers that the crystallites decrease in size as the deformation increases up to 0.00064.

In the case of the Pt-doped catalyst, the peaks coincide with the crystalline planes of the 56.93° (1 0 -1) and 66.35° (2 0 0) facets of Pt according to the COD-1001824 standard for Pt where the intensity of the peaks increased with increasing Pt concentration. The average crystal size obtained was 57.21340 nm, which is larger than the crystal size of ZnO due to the addition of the metallic compound. The maximum achieved crystal deformation was 0.00037.

No peak shifts are observed when Pt is loaded on the ZnO surface, indicating that the Pt particles do not modify the crystal structure of ZnO [45].

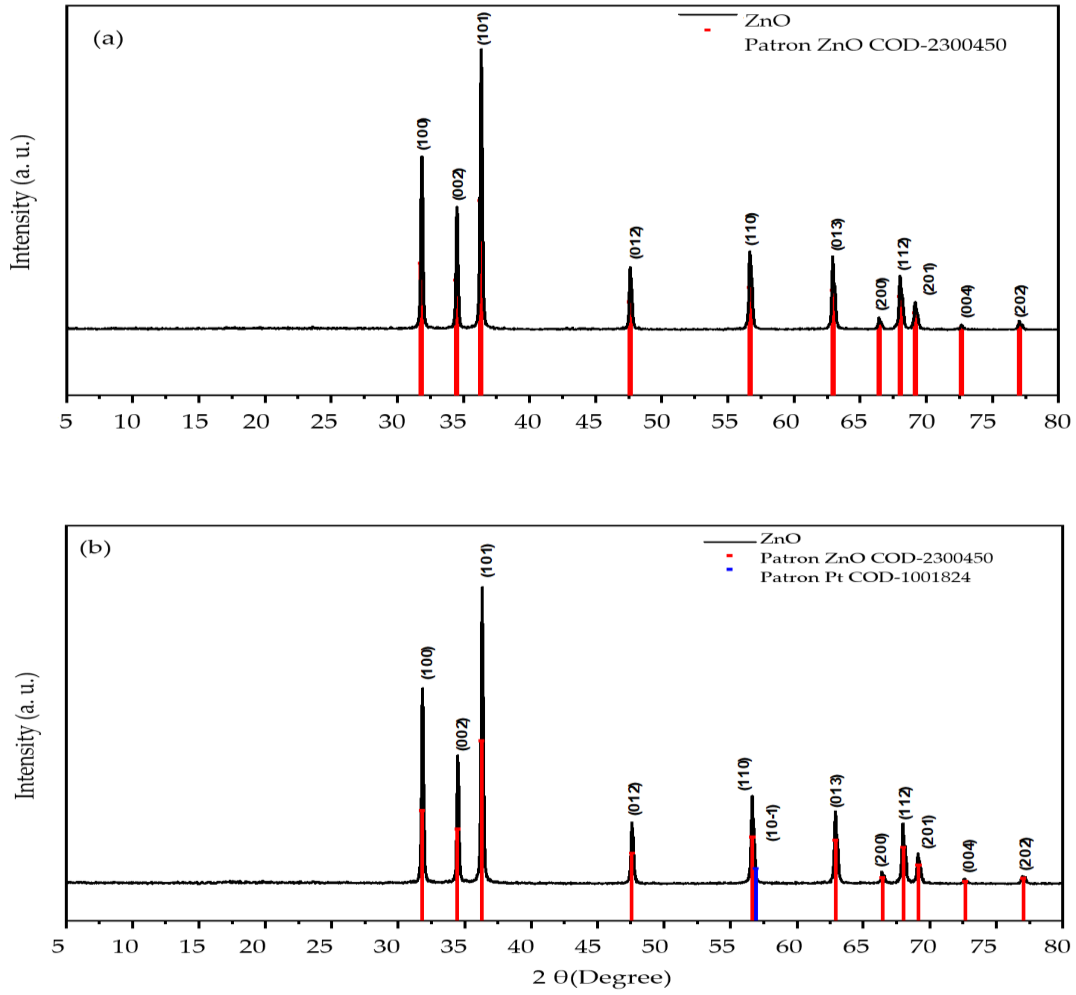

Figure 2. XRD of the synthesis of (a) ZnO and (b) Pt-ZnO.

The SEM micrograph of the synthesized ZnO and Pt-ZnO NPs can be seen in Figures 3a and 3b, respectively. Figure 3a reveals the morphology and size of the ZnO particles, which do not present a homogeneous structure due to the synthesis method used (precipitation method), as observed in the distribution graphic. The material presents a hexagonal shape with an average diameter of 114.10 nm.

Figure 3b shows the morphology obtained from the synthesis of Pt- ZnO, which has a rod shape with a homogeneous distribution and an average diameter of 99.70 nm. A change of structure was observed when platinum was added to the semiconductor by the wet impregnation method. This structure is one of the best for photocatalytic processes compared to other types of morphologies, such as spherical or hexagonal, because it exposes an enlarged active surface, which increases the sites available for the adsorption of reagents (e.g., organic pollutants or water molecules) and interaction with light. The elongated morphology facilitates the directional movement of electrons along the longitudinal axis of the rod, reducing electron-hole pair recombination. Since they are one-dimensional structures that provide more efficient carrier transport due to decreased surface defects, the exposed crystalline faces on nanowires are usually more reactive. These faces generated oxidizing species (such as -OH) and facilitated charge transfer, thereby enhancing photocatalytic activity.it is a one-dimensional structure that provides more efficient carrier transport due to the decrease in surface defects, disorder, and discontinuous interfaces [46].

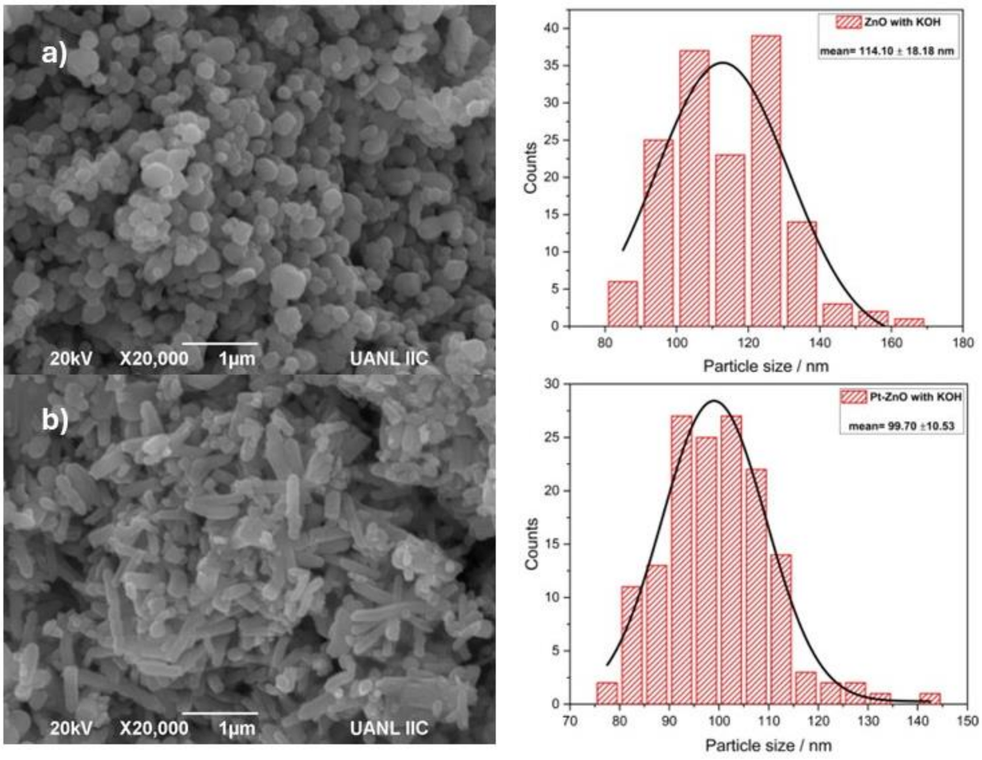

Figure 3. SEM images and particle size distribution of a) ZnO at 2000x and of b) Pt-ZnO at 2000x.

2.2. Kinetic Analysis

This indicates that photocatalytic oxidation reactions follow Langmuir-Hinshelwood-Hougen-Watson (LH-HW) type kinetics [47–50] as follows:

$$-r_a = -\frac{dC}{dt} = \frac{K_1 C}{1+K_2 C+\sum K_i C_i} \quad (1)$$

Where: K_1C represents the kinetic term of the rate equation, K_2C represents the adsorption term of the reactant, and $\sum(K_i\ C_i)$ represents the adsorption term of all the intermediate products of the degradation reaction of organic compounds.

If the experimental data are analyzed at very short reaction times, the adsorption term of the intermediate products can be neglected.

Based on the above, it can be shown that the following equation can represent the general kinetic form:

$$r_a = -\frac{dC}{dt} = \frac{K_1 C^m}{1+K_2 C^n} \quad (2)$$

If the exponents m and n have a value of 1, the constants K_1 and K_2 can be determined directly from the graph of reaction rate versus concentration.

Equation (2) can be linearized in the manner recommended by Fogler [49] and Moctezuma [47], using the following initial conditions: t=0, C= C_0, and reaction rate, the following equations are obtained:

$$r_a|_{t=0} = \frac{K_1 C_0}{1+K_2 C_0} \quad (3)$$

$$\frac{1}{-r_a|_{t=0}} = \frac{1+K_2 C_0}{K_1 C_0} = \frac{1}{K_1 C_0} = \frac{K_2 C_0}{K_1 C_0} \quad (4)$$

$$\frac{1}{-r_a|_{t=0}} = \frac{1}{K_1 C_0} + \frac{K_2}{K_1} \quad (5)$$

Equation (5) 's behavior is represented in Figure 9, where the ordinate at the origin is K_2/K_1, and the slope is given by $1/K_1$.

$$-r_{AC} = -\frac{dC_{AC}}{dt} = \frac{K_1 C_{AC}}{1 + K_2 C_{AC}} \quad (6)$$

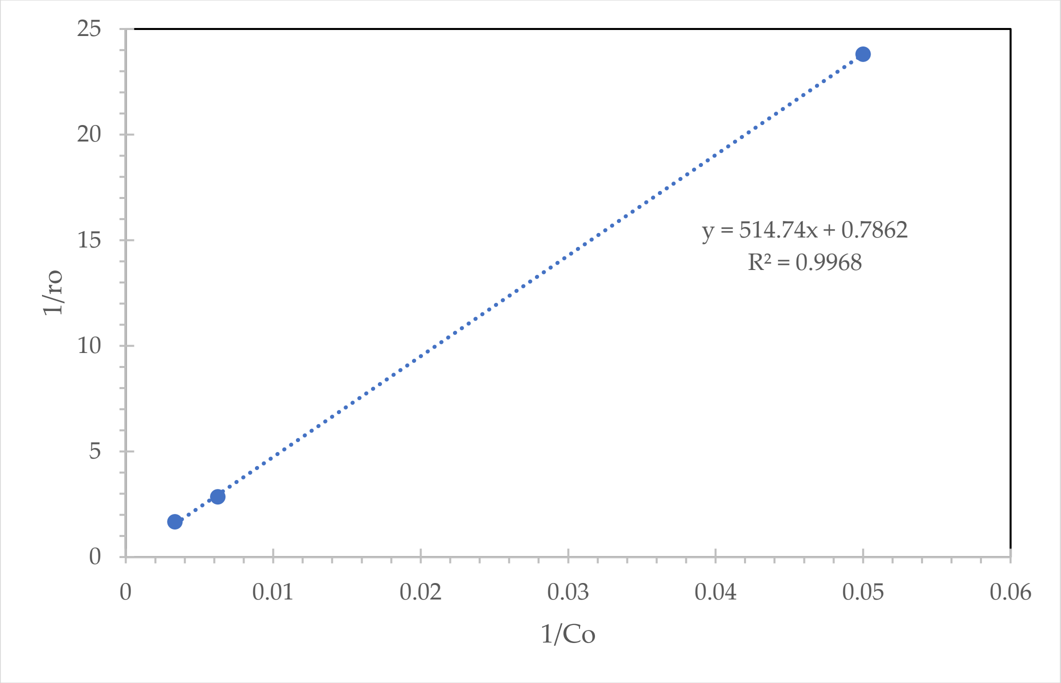

Figure 4. Graph of 1/ro vs. 1/Co to obtain the K_1 and K_2 values of the LH-HW model.

From the values obtained in Figure 9, we have the values of the constants, and therefore, the previous equation is expressed as follows:

$$-r_{AC} = \frac{0.0019 * C_{PY}}{1 + 0.0015 * C_{PY}} \quad (7)$$

The values of the reaction constants $k_1 = 0.0019$ min^{-1} are low if we compare them with the results presented by Leyva [51], but the system was a 300 mL reactor, and the catalyst was only zinc oxide where pyridine was degraded using UV lamps, and the absorption constant $k_2 = 0.0015$ L/mg is slightly lower than the results presented by this author, but it can be said that the absorption of pyridine is not favorable in this system, since most of the reaction is due to the formation of hydroxyl radicals.

Figure 5 shows the behavior of the LH-HW model of the experimental data and the model. The data is observed to have a behavior similar to the model, adjusting to its behavior.

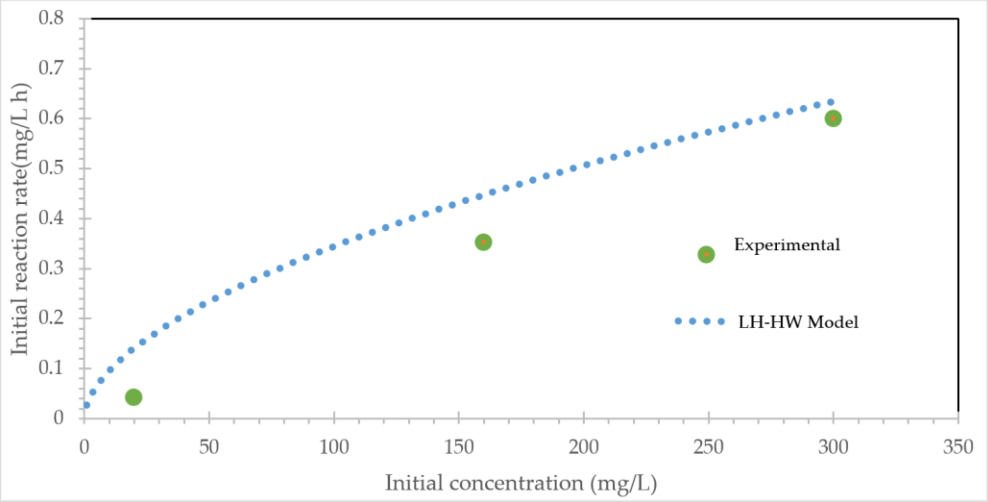

Figure 5. Initial reaction rate as a function of initial concentration (300 min of reaction using 15-watt natural light lamps, using ZnO-Pt as a catalyst).

Figure 6 shows the influence of pH, pyridine concentration, and amount of catalyst on the kinetic constant *k* in the degradation of pyridine. It can be observed that at an acid pH (pH 4) the *k* is high; this can be attributed to a more significant generation of hydroxyl radicals (·OH) and a better adsorption of pyridine on the catalyst surface, as the pH increases (pH 7-10) the constant *k* tends to decrease, this could be due to an electrostatic repulsion between the catalyst surface and the anionic species formed at high pH.

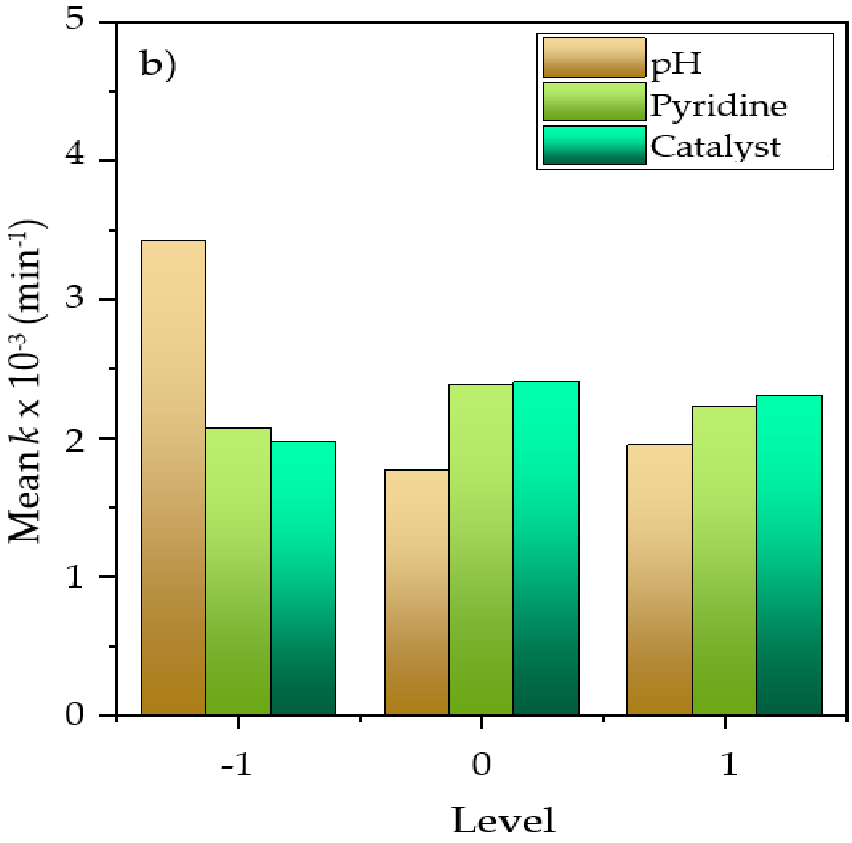

Figure 6. Influence of pH, pyridine concentration, and amount of catalysts on the kinetic constant.

2.3. Evaluation of Critical Variables in Pyridine Removal by DOE

A Box-Behnken design of experiments was implemented to optimize pyridine degradation in aqueous solutions, enabling the modeling and understanding of the interactions between the studied factors with a limited number of experiments. The results obtained are presented below. Figure 7 shows the Pareto chart, a statistical tool that enables us to identify and prioritize the factors most significantly influencing a pyridine removal process. As can be seen, the factor with the most significant impact is pH, along with its quadratic term. This effect is due to the pH of the medium being a determining factor in the removal of organic compounds such as pyridine. Previous work has shown that a pH close to neutral favors the generation of hydroxyl radicals (·OH), highly reactive species responsible for oxidation reactions.

Furthermore, pH directly affects the surface charge of the catalyst and the ionization of the organic compound, thereby influencing the compound's adsorption. Shu et al. achieved efficient photocatalytic degradation of pyridine using TiO_2 modified with La and Fe at a pH of 8. They attribute this efficiency to improved adsorption of pyridine on the catalyst and more significant generation of reactive species under slightly alkaline conditions [52]. The Pareto diagram indicates that the factors do not act independently in the degradation of pyridine. That is, there are important interactions between the factors, for example, AC and AB.

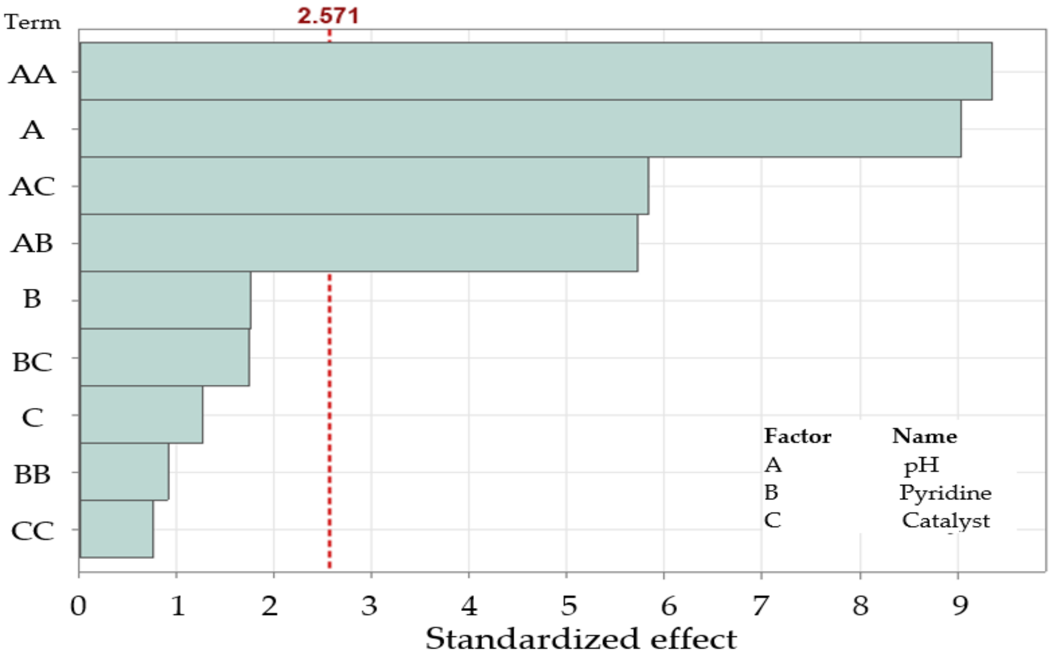

Figure 7. Standardized Pareto chart on statistical significance of main effects and interactions in pyridine removal.

Figure 8 shows how each factor individually influences the photocatalytic removal of pyridine. It has been confirmed that pH is the most significant factor influencing the process. As mentioned above, an adequate pH level optimizes the generation of hydroxyl radicals (·OH) [53]. Likewise, pH affects the surface charge of the catalyst and improves pyridine adsorption by ionizing it. The figure also shows that the pyridine and catalyst factors do not have a marked effect within the study range. However, it is observed that the initial pyridine concentration directly influences its removal. At low pyridine concentrations, there is greater availability of active sites on the catalyst for pyridine adsorption, which facilitates its oxidation. However, at higher concentrations, the active sites may become saturated, and the accumulation of intermediates may inhibit the process. Meanwhile, a high amount of catalyst ensures a more significant number of active sites, which are responsible for generating reactive species and a larger adsorption surface area [54].

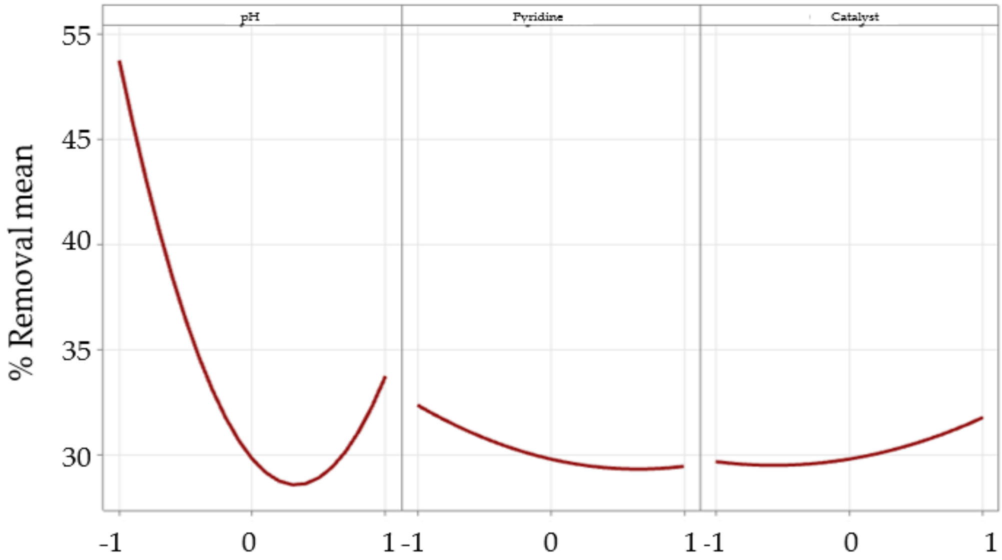

Figure 8. Main effects of pH, pyridine concentration, and catalyst loading on pyridine removal efficiency.

Figure 9 illustrates the interactions corresponding to the different levels of the studied factors. Figure 11a shows that high levels of pyridine require an acidic pH to enhance pyridine degradation; this is because, at acidic pH, pyridine is protonated, producing the pyridine ion (PyH^+), which increases its solubility for its degradation and adsorption processes [55]. In Figure 11b, it can be observed that the highest percentage of pyridine degradation occurs at low pH levels. At high catalyst levels, this interaction is attributed to the fact that pH influences the generation of reactive species, such as hydroxyl radicals (·OH), which are responsible for the oxidation of pyridine. As can be seen, at high pH levels, the efficiency of degradation decreases; this could be due to the precipitation of the metallic species present in the catalyst [53]. A high catalyst level improves the availability of active sites for the generation of reactive species. Figure 11c shows an optimal concentration range for pyridine and the catalyst. Excessive amounts of pyridine can saturate the catalyst's active sites, while increased amounts of catalyst can cause particle agglomeration and light obstruction, reducing process efficiency.

Preprints.org (www.preprints.org) | NOT PEER-REVIEWED | Posted: 23 June 2025 doi:10.20944/preprints202506.1830.v1

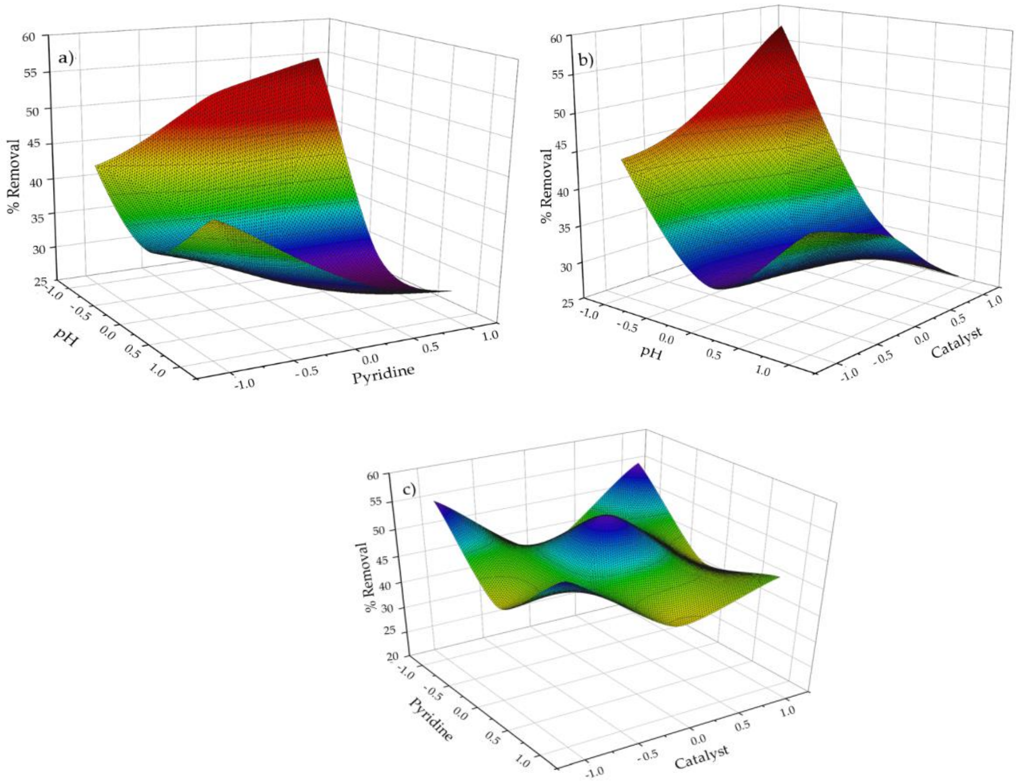

Figure 9. Response surface plots: The interaction effects of operational parameters on pyridine degradation efficiency, a) pH-pyridine interaction, b) pH-catalyst interaction, and c) pyridine-catalyst interaction.

A polynomial regression model was developed to represent the percentage of pyridine removal as a function of the process input variables (pH, initial pyridine concentration, and catalyst). The calculated regression model is presented in Equation 8, which provides an adequate fit to the experimental data ($R^2 = 0.943$).

$$\%\mathrm{Removal} = 29.80 - 7.497\mathrm{pH} - 1.453\mathrm{P} + 1.049\mathrm{C} + 11.43\mathrm{pH}^2 + 1.11\mathrm{P}^2 + 0.93\mathrm{C}^2 - 6.72\mathrm{pH}\cdot\mathrm{P} - 6.85\mathrm{pH}\cdot\mathrm{C} - 2.03\mathrm{P}\cdot\mathrm{C} \quad (8)$$

Figure 10, pH, shows the normal probability plot, which evaluates the assumption of a normal distribution in the fitted regression model. It can be seen that most of the points are close to the red line, indicating that the normality of the residuals is met, although there are a few residual points that are slightly off the scale but not enough to invalidate the model.

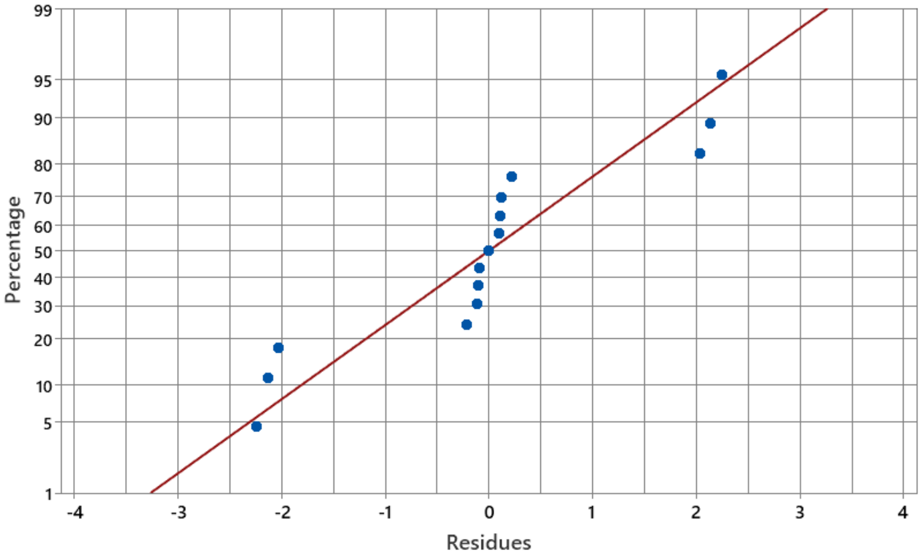

Figure 10. Normal probability plot of model residuals for % pyridine degradation.

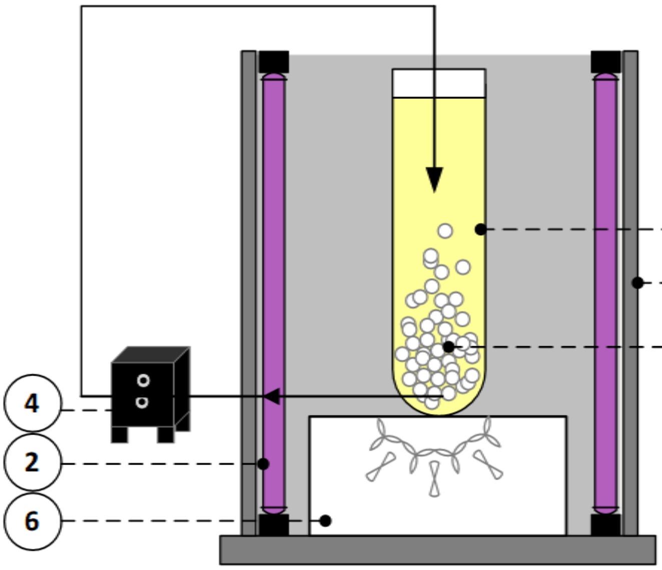

Figure 11. Diagram of fluidized bed photocatalytic reactor cross-sectional view: (1) Reactor body, (2) UV lamps, (3) Reactor cell, (4) Recirculation pump, (5) Catalyst bed, (6) Blower.

3. Methodology

3.1. *Chemical Products and Reagents*

The reagents used to carry out the synthesis of the catalyst were: zinc nitrate hexahydrate (Zn $(NO_3)_2{\cdot}6H_2O$) with 99% purity purchased from Meyer, potassium hydroxide (KOH) with 85% purity purchased from Meyer, platinum acetylacetonate ($C_{10}H_{14}O_4Pt$) with 97% purity obtained from Sigma-Aldrich, and acetone ($(CH_3)_2CO$) 99.6% purity purchased from JT Baker. The following reagents for photoactivity evaluation of the catalyst were used: Pyridine (C_5H_5N) was obtained from Sigma-Aldrich, and distilled water was obtained from Wöhler (reagent grade).

3.2. *Photocatalyst Preparation*

The synthesis of the semiconductor zinc oxide (ZnO) was carried out by the direct precipitation method [44]. Two solutions were prepared: zinc nitrate (0.2 M) and potassium hydroxide (0.4 M), both in distilled water as the solvent. The potassium hydroxide solution was added to the zinc nitrate solution by magnetic stirring. The mixture was left to stand for 20 min, filtered under vacuum, and the precipitate obtained was washed with distilled water and ethanol to remove impurities. Finally, it was dried at 100°C for 24 h and calcined at 500°C for three hours.

The doping of ZnO with platinum nanoparticles (Pt-ZnO) was performed using the incipient impregnation technique [41] by the following steps: A 0.5 wt.% platinum acetylacetonate solution diluted in acetone was prepared and added on ZnO over a heating grid at 90 °C for subsequent calcination in muffle at 400 °C for two hours.

The Pt-ZnO was supported on alumina (Al_2O_3) using the wet impregnation technique [41]. A solution of 3 g of Pt-ZnO was prepared in 250 mL of distilled water, which was added to the Al_2O_3 beads by stirring for 30 minutes. The mixture of the Pt-ZnO solution and the alumina beads was left under UV irradiation for 24 hours to achieve maximum adsorption of the semiconductor onto the support. Finally, the calcination of the support was carried out in the flask at 550°C for three hours.

3.3. Photocatalyst Characterization

Fourier transform infrared spectroscopy (FTIR) analysis was performed using the Agilent Cary 660 spectrometer with a scanning range of 4000 to 400 cm^{-1} with attenuated total reflectance (ATR) to verify the presence of ZnO and Pt. To evaluate the crystal structure of the synthesized photocatalyst, a Rigaku Ultima IV diffractometer with a thin film module (Cu radiation $K\alpha$ $\lambda = 0.15418$ nm, 40 kV, 44 mA and angle step of 0.02°) in Bragg-Brentano configuration was used [56]. Subsequently, the results obtained were analyzed with Match! 3.3 Software. The morphology and size distribution of the nanoparticles of Pt-ZnO/Al_2O_3 NPs were analyzed by scanning electron microscopy (SEM) with INSTRUMENT JSM-6490 equipment at a voltage of 20 kV and a magnification of 20000x. The micrographs were interpreted in ImageJ software to determine the approximate size of the NPs.

3.4. Fluidized Bed Photocatalytic Reactor Used for Photocatalytic Experiments

A fluidized bed photocatalytic reactor was used for the pyridine degradation runs; this reactor consists of a borosilicate glass cell of 5 cm in diameter and 50 cm in length, with an adequate volume of 500 mL; the external body of the reactor is made of stainless steel, resistant to corrosive conditions; its diameter measures 31 cm and 56 cm in length, Pt constitutes the reactor bed- ZnO/ Al_2O_3 photocatalyst beads. A Mayware fan was installed to lower the temperature within the reaction, thereby minimizing the impact on the photocatalytic process. Two UV lamps with a wavelength (λ) of 365 nm and 15 watts were placed inside the reactor housing; a recirculation pump was also placed to circulate the solution countercurrent through the system. Figure 11 shows the diagram of the fluidized bed reactor. In Figure 12, we can appreciate the image of the photoreactor with catalyst specifications described in Figure 11.

For the construction of the reactor cell, it was considered that the material to be used should be transparent to UV radiation; quartz is an ideal material due to its good UV light transmittance and chemical and thermal resistance. However, its high price limits its application in photocatalysis for this project; therefore, it was decided to use borosilicate glass, which has an excellent transmittance for UV light.

One of the critical parameters to take into account is the diameter of the reactor, which must be considered in order to have a balance between the illumination, the amount of catalyst, and the solution. In tubular photoreactors, practical diameters generally range from 25 to 50 mm. Smaller diameters can result in a high-pressure drop, while larger diameters will have less volume illumination, which decreases the process efficiency. Therefore, the reactor was built with a diameter of 5 cm and a length of 50 cm, which allowed working with considerable amounts of charge with the maximum possible number of useful photons reaching the cell, and the volume would guarantee monitoring the dissolution, evaluating the phenomenological behavior of the pyridine in contact with the catalyst. In Figure 12, we can see the actual image of the photoreactor with specifications described in Figure 11.

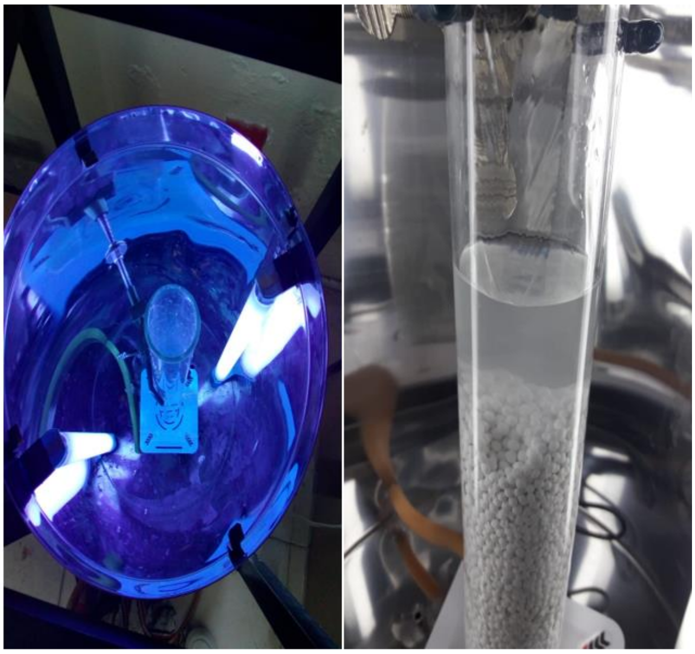

Figure 12. Top view and front view of fluidized bed photocatalytic reactor**.**

3.5. Photocatalytic Experiments

The pyridine degradation runs were carried out following a Box-Behnken-type experimental design (Table 1) where the independent variables were the following: pyridine concentration (20 ppm, 160 ppm, and 300 ppm), amount of catalyst (20, 60, and 100 g), and pH (4, 7, and 10), under normal conditions of pressure and temperature (1 atm, 27°C). The percentage of pyridine degradation was measured as a response variable. These conditions simulate wastewater discharges from industries that manufacture pyridine and its derivatives [9]. The pH and catalyst amount conditions were used to analyze their effect during the photocatalytic process.

Table 1. Experimental design.

	Coded variables			Natural variables		
Experiments	**pH (-)**	**Concentration (ppm)**	**Time (min)**	**pH (-)**	**Concentration (ppm)**	**Time (min)**
1	-1	0	-1	3	160	120
2	-1	-1	0	3	20	240
3	0	0	0	6	160	240
4	0	-1	-1	6	20	120
5	-1	0	1	3	160	360
6	0	0	0	6	160	240
7	1	0	1	9	160	360
8	-1	1	0	3	300	240
9	1	0	-1	9	160	120
10	0	-1	1	6	20	360
11	1	-1	0	9	20	240
12	0	1	1	6	300	360
13	0	0	0	6	160	240
14	0	1	-1	6	300	120
15	1	1	0	9	300	240

Samples were taken every 30 minutes for 4 hours to measure the concentration of pyridine inside the photoreactor. Each sample was analyzed in a UV-VIS VE-5100UV VELAB UV-VIS spectrometer.

4. Conclusions

The experimental results obtained from the degradation runs show that pH was the most influential factor in the degradation process, i.e., acidic conditions maximize efficiency, as well as moderate pyridine concentration and high catalyst loading. However, high concentrations over time saturate the active sites, leading to agglomeration and reduced light penetration.

The fluidized bed reactor demonstrated improved mass transfer, enhanced catalytic exposure to UV light, and catalyst stability, which is ideal for treating wastewater with recalcitrant contaminants. The Pt-ZnO/Al_2O_3 catalyst in an FBR obtained high efficiency, stability, and potential to degrade pyridine in industrial effluents. Its nano-barrier morphology and synergy with the FBR offer a promising solution for N-heterocycles, which may lay the foundation for industrial-scale applications.

Author Contributions: For research articles with several authors, a short paragraph specifying their individual contributions must be provided. The following statements should be used “Conceptualization, R. G. and C. M.; methodology, R. G. and C. M; formal analysis, R. G. and C. M.; investigation, R. G. and C. M.; resources, R. G. and C. M.; data curation, S. G.; writing—original draft preparation, R. G; writing—review and editing, R. G. and C. M; visualization, G. L.; supervision, S. G.; project administration, R. C., J. C. and A. G.; funding acquisition, D. M. and G. L. All authors have read and agreed to the published version of the manuscript.” Please turn to the CRediT taxonomy for the term explanation. Authorship must be limited to those who have contributed substantially to the work reported.

Data Availability Statement: Suggested Data Availability Statements are available in section “MDPI Research Data Policies” at https://www.mdpi.com/ethics.

Acknowledgements: Author R. S. Ginés-Palestino appreciates the support of the Secretariat for Science, Humanities, Technology and Innovation (Secihti) for a scholarship granted with key number 508410. The co-authors also thank the State Government of Veracruz de Ignacio de la Llave and the Veracruz Council for Scientific Research and Technological Development (COVEICyDET) for funding this project with the number 15 002.

Conflicts of Interest: “The authors declare no conflicts of interest.” “The funders had no role in the design of the study; in the collection, analyses, or interpretation of data; in the writing of the manuscript; or in the decision to publish the results”.

References

1. Rajput, M.S. and B. Mishra, *Biodegradation of pyridine raffinate using bacterial laccase isolated from garden soil.* Biocatalysis and Agricultural Biotechnology, 2019. **17**: p. 32-35.
2. Swain, A.K., A. Sahoo, H.M. Jena, and H. Patra, *Industrial wastewater treatment by aerobic inverse fluidized bed biofilm reactors (AIFBBRs): a review.* Journal of Water Process Engineering, 2018. **23**: p. 61-74.
3. Sahu, D., et al., *Advances in synthesis, medicinal properties and biomedical applications of pyridine derivatives: A comprehensive review.* European Journal of Medicinal Chemistry Reports, 2024: p. 100210.
4. Huang, D., et al., *Enhancement of the quinoline separation from pyridine: study on competitive adsorption kinetics in foam fractionation with salt.* Chemical Engineering Journal, 2019. **359**: p. 1150-1158.
5. Amin, A., et al., *A review on the medicinal and industrial applications of N-containing heterocycles.* The Open Medicinal Chemistry Journal, 2022. **16**(1).
6. Lu, Q., et al., *Bioavailable electron donors leached from leaves accelerate biodegradation of pyridine and quinoline.* Science of the Total Environment, 2019. **654**: p. 473-479.
7. Feng, J., W.-C. Geng, H. Jiang, and B. Wu, *Recent advances in biocatalysis of nitrogen-containing heterocycles.* Biotechnology Advances, 2022. **54**: p. 107813.
8. Chu, L., S. Yu, and J. Wang, *Degradation of pyridine and quinoline in aqueous solution by gamma radiation.* Radiation Physics and Chemistry, 2018. **144**: p. 322-328.

9. Zalat, O. and M. Elsayed, *A study on microwave removal of pyridine from wastewater.* Journal of Environmental Chemical Engineering, 2013. **1**(3): p. 137-143.
10. Montalvo, C., et al., *Fluidized bed photoreactor for the removal of acetaminophen and pyridine using Al-doped TiO2 supported on alumina.* Iranian Journal of Catalysis, 2022. **12**(3).
11. Program, N.T., *NTP technical report on the toxicology and carcinogenesis studies of pyridine (CAS no. 110-86-1) in F344/N rats, Wistar rats, and B6C3F1 mice (drinking water studies).* 2000.
12. Goswami, S., et al., *Recent trends in the synthesis, characterization and commercial applications of zinc oxide nanoparticles-a review.* Inorganica Chimica Acta, 2024: p. 122350.
13. Tarannum, N. and D. Kumar, *Pyridine: Exposure, risk management, and impact on life and environment*, in *Hazardous Chemicals*. 2025, Elsevier. p. 363-374.
14. Khan, K.M., S.S. Gillani, and F. Saleem, *Role of pyridines as enzyme inhibitors in medicinal chemistry*, in *Recent Developments in the Synthesis and Applications of Pyridines*. 2023, Elsevier. p. 207-252.
15. Wu, J., et al., *Biodegradation: the best solution to the world problem of discarded polymers.* Bioresources and Bioprocessing, 2024. **11**(1): p. 79.
16. Choudhary, M., et al., *Environmental issues: a challenge for wastewater treatment.* Green materials for wastewater treatment, 2020: p. 1-12.
17. Jaramillo-Páez, C., J.A. Navío, M. Hidalgo, and M. Macías, *ZnO and Pt-ZnO photocatalysts: Characterization and photocatalytic activity assessing by means of three substrates.* Catalysis Today, 2018. **313**: p. 12-19.
18. Gines-Palestino, R., E. Oropeza-De la Rosa, C. Montalvo-Romero, and D. Cantú-Lozano, *Rheokinetic and effectiveness during the phenol removal in mescal vinasses with a rotary disks photocatalytic reactor (RDPR) Reocinética y efectividad durante la remoción de fenol en vinazas de mezcal con un reactor fotocatalítico de discos rotativos (RDPR).*
19. López- Ojeda, G.C., et al., *Oxidación fotoelectrocatalítica de fenol y de 4-clorofenol con un soporte de titanio impregnado con TiO2.* Revista internacional de contaminación ambiental, 2011. **27**(1): p. 75-84.
20. Jing, Y., et al., *Fabrication of Pt doped TiO2–ZnO@ ZIF-8 core@ shell photocatalyst with enhanced activity for phenol degradation.* Environmental Research, 2022. **203**: p. 111819.
21. Priyadarshini, M., I. Das, M.M. Ghangrekar, and L. Blaney, *Advanced oxidation processes: Performance, advantages, and scale-up of emerging technologies.* Journal of environmental management, 2022. **316**: p. 115295.
22. Deng, Y. and R. Zhao, *Advanced oxidation processes (AOPs) in wastewater treatment.* Current pollution reports, 2015. **1**(3): p. 167-176.
23. Ibigbami, B., et al., *Advanced oxidation processes: a supplementary treatment option for recalcitrant organic pollutants in Abattoir wastewater.* Journal of applied research and technology, 2023. **21**(6): p. 1019-1041.
24. Domènech, X., W.F. Jardim, and M.I. Litter, *Procesos avanzados de oxidación para la eliminación de contaminantes.* Eliminación de contaminantes por fotocatálisis heterogénea, 2001. **2016**: p. 3-26.
25. Bello, M.M., A.A.A. Raman, and M. Purushothaman, *Applications of fluidized bed reactors in wastewater treatment–a review of the major design and operational parameters.* Journal of Cleaner Production, 2017. **141**: p. 1492-1514.
26. Michaelides, E.E.S., *Heat and mass transfer in particulate suspensions.* 2013.
27. Cai, Q., B. Lee, S. Ong, and J. Hu, *Fluidized-bed Fenton technologies for recalcitrant industrial wastewater treatment–Recent advances, challenges and perspective.* Water Research, 2021. **190**: p. 116692.
28. An, Q., J. Li, J. Peng, and L. Hu, *Dissolved gas analysis in transformer oil using Pd, Pt doped ZnO: A DFT study.* Chemical Physics Letters, 2025. **868**: p. 142018.
29. Shubha, J., et al., *Facile synthesis of ZnO/CuO/Eu heterostructure photocatalyst for the degradation of industrial effluent.* Arabian Journal of Chemistry, 2023. **16**(3): p. 104547.
30. Sun, Y., et al., *Preparations and applications of zinc oxide based photocatalytic materials.* Advanced Sensor and Energy Materials, 2023. **2**(3): p. 100069.
31. Gatou, M.-A., et al., *ZnO nanoparticles from different precursors and their photocatalytic potential for biomedical use.* Nanomaterials, 2022. **13**(1): p. 122.
32. Güell, F., et al., *ZnO-based nanomaterials approach for photocatalytic and sensing applications: recent progress and trends.* Materials Advances, 2023. **4**(17): p. 3685-3707.

33. Dey, S. and G. Dhal, *Property and structure of various platinum catalysts for low-temperature carbon monoxide oxidations.* Materials Today Chemistry, 2020. **16**: p. 100228.
34. Wang, X., et al., *Structural Regulation of Advanced Platinum-Based Core-Shell Catalysts for Fuel Cell Electrocatalysis.* Minerals, 2025. **15**(3): p. 235.
35. Marturano, M., E. Aglietti, and O. Ferretti, *α-Al2O3 catalyst supports for synthesis gas production: Influence of different alumina bonding agents on support and catalyst properties.* Materials chemistry and physics, 1997. **47**(2-3): p. 252-256.
36. Wang, Y., et al., *Regulating the coordination environment of surface alumina on NiMo/Al2O3 to enhance ultra-deep hydrodesulfurization of diesel.* Applied Catalysis B: Environment and Energy, 2024. **357**: p. 124265.
37. Lee, J.K., et al., *Platinum-tin nano-catalysts supported on alumina for direct dehydrogenation of n-butane.* Journal of Nanoscience and Nanotechnology, 2015. **15**(10): p. 8305-8310.
38. Huang, X., et al., *Fabrication of highly efficient ZnO-Pt catalysts assisted by biomass-derived carboxymethyl cellulose for the photodegradation of diverse antibiotics.* Journal of Environmental Management, 2025. **382**: p. 125418.
39. Ishikawa, T., K. Matsumoto, K. Kandori, and T. Nakayama, *Synthesis of layered zinc hydroxide chlorides in the presence of Al (III).* Journal of Solid State Chemistry, 2006. **179**(4): p. 1110-1118.
40. Nie, C., L. Liu, and R. He, *Pt/TiO2-ZnO in a circuit Photo-electro-catalytically removed HCHO for outstanding indoor air purification.* Separation and Purification Technology, 2018. **206**: p. 316-323.
41. González Vera, O.F., J.J. Mutiz, and J. Urresta Aragón, *Synthesis and characterization of Cu type catalysts supported on MgO, SiO 2, ZnO, and Al 2 O 3 applied to the hydrogenolysis of glycerol.* Revista ION, 2017. **30**(2): p. 31-41.
42. Manikandan, B., K. Murali, and R. John, *Optical, morphological and microstructural investigation of TiO2 nanoparticles for photocatalytic application.* Iranian Journal of Catalysis, 2021. **11**(1).
43. Manikandan, A., J.J. Vijaya, L.J. Kennedy, and M. Bououdina, *Structural, optical and magnetic properties of Zn1− xCuxFe2O4 nanoparticles prepared by microwave combustion method.* Journal of molecular structure, 2013. **1035**: p. 332-340.
44. Gines-Palestino, R.S., et al., *Microstructural, Morphological, and Optical Study of Synthesis of ZnO and Pt ZnO Nanoparticles by a Simple Method Using Different Precipitating Agents.* Journal of the Brazilian Chemical Society, 2024. **35**(1): p. e-20230092.
45. Hong, D., et al., *Construction of a Pt-modified chestnut-shell-like ZnO photocatalyst for high-efficiency photochemical water splitting.* Electrochimica Acta, 2018. **283**: p. 959-969.
46. Morkoç, H. and Ü. Özgür, *Zinc oxide: fundamentals, materials and device technology*. 2008: John Wiley & Sons.
47. Moctezuma E., López M., Zermeño B. Reaction pathways for the photocatalytic degradation of phenol under different experimental conditions. *Revista Mexicana de Ingeniería Química*. **2016**, *15,* 1,129-137
48. 48. Montalvo, C., Aguilar, C., Alcoser, R., et al. Semi-Pilot Photocatalytic Rotating Reactor (RFR) with Supported TiO_2/Ag Catalysts for Water Treatment. *Molecules*, 2018, *23*(1), 224. https://www.ncbi.nlm.nih.gov/pmc/articles/PMC6017124/.
49. Fogler, H.S. Elements of Chemical Reaction Engineering. Prentice Hall, N. J. USA. 1, 2021.
50. Matthews, Ralph W and McEvoy Stephen R. Photocatalytic degradation of phenol in the presence of near-UV illuminated titanium dioxide. *J. Photochem. Photobiol. A*. **1992**, *64*, 2, 231-246. https://doi.org/10.1016/1010-6030(92)85110-G
51. Leyva Elisa, Montalvo Carlos, Moctezuma Edgar * and Leyva Socorro. Photocatalytic degradation of pyridine in water solution using ZnO as an alternative catalyst to TiO_2. J. Ceramic Processing Res. 2008, 9, 455-462.
52. Shu, J., et al., *Influencing Factors and Kinetics of Modified Shell Powder/La-Fe-TiO_2 Photocatalytic Degradation of Pyridine Wastewater.* International Journal of Environmental Research and Public Health, 2022. **19**(22): p. 14835.
53. Bensalah, N., M.I. Ahmad, and A. Bedoui, *Catalytic degradation of 4-ethylpyridine in water by heterogeneous photo-Fenton process.* Applied Sciences, 2019. **9**(23): p. 5073.

54. Gosu, V., S. Arora, and V. Subbaramaiah, *Simultaneous degradation of nitrogenous heterocyclic compounds by catalytic wet-peroxidation process using box-behnken design.* Environmental Engineering Research, 2020. **25**(4): p. 488-497.
55. Sadiq, M. and S. Hussian, *An efficient activated carbon for the wastewater treatment, prepared from peanut shell.* Modern Research in Catalysis, 2013. **2**(4): p. 148-156.
56. Amador-Gómez, L.P., et al., *Synthesis, Modification, and Characterization of* Fe_3O_4*@* SiO_2*-PEI-Dextranase Nanoparticles for Enzymatic Degradation of Dextran in Fermented Mash.* Processes, 2022. **11**(1): p. 70.